Graphical Abstract

Experimental investigation of the hydro-elastic response of a spar-type floating offshore wind turbine

V. Leroy,S. Delacroix,A. Merrien,E. E. Bachynski-Polić,J.-C. Gilloteaux

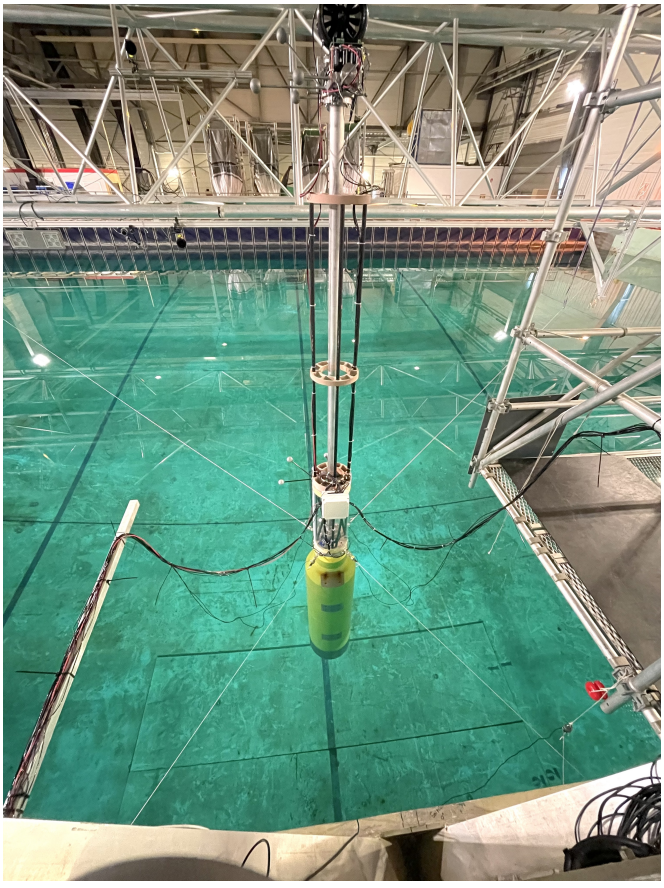

Highlights

Experimental investigation of the hydro-elastic response of a spar-type floating offshore wind turbine

V. Leroy,S. Delacroix,A. Merrien,E. E. Bachynski-Polić,J.-C. Gilloteaux

- Experimental modelling of a 10 MW floating offshore wind turbine supported by a spar platform, including flexibility of the platform.
- The first flexible bending mode frequency of the spar and tower is Froude scaled.
- A resonant response of the first bending mode of the platform was observed in regular waves. This response was triggered by nonlinear hydrodynamic loads (2^{nd} to 4^{th}-order).
- In irregular waves, ringing/springing response of the turbine was measured, particularly in moderate sea-states with short peak periods, or in strong and steep sea-states with large peak periods.

Experimental investigation of the hydro-elastic response of a spar-type floating offshore wind turbine

V. Leroy[a,*], S. Delacroix[a], A. Merrien[a], E. E. Bachynski-Polić[b] and J.-C. Gilloteaux[a]

[a]LHEEA, Centrale Nantes/CNRS, 1 rue de la Noë 44300 Nantes, France
[b]Department of Marine Technology, NTNU, 7491 Trondheim, Norway

ARTICLE INFO

Keywords:
Experiments
Floating Offshore Wind Turbines
Hydro-elasticity
Nonlinear hydrodynamics
Springing/ringing

ABSTRACT

As the size of floating wind turbines continues to increase, floating platforms reach dimensions that make their elastic and hydro-elastic behaviour significant. Several works in connection with the numerical modelling of the elastic behaviour of these wind turbines have been carried out but few validation data are available. This study focuses on the hydro-elastic response of a large floating wind turbine, in regular waves and severe sea-states. A new experimental wind turbine model has been designed to represent a 1:40 Froude-scaled spar platform carrying the DTU 10 MW turbine. The main challenge is here to reproduce a 1st bending mode frequency and hydrodynamic loads representative of a realistic large floating wind turbine. The platform model is made of a flexible backbone, reproducing the correct flexibility, and light floaters fixed on it provide the correctly scaled geometry. This experimental model is tested in various conditions including regular waves of several periods and steepness, and irregular waves of various intensity, including extreme 50-year return period conditions. Highly nonlinear hydroelastic responses are observed in regular waves when higher order hydrodynamic loads excite the bending mode. In irregular sea-states, this behaviour was also triggered by strongly nonlinear effects resulting in a springing or ringing response of the system. This highlights the importance of nonlinear hydrodynamics in hydro-elastic analysis of large floating wind turbines. Eventually, the collected database could be relevant for a more advanced analysis with comparison to both linear and nonlinear hydro-elastic simulation tools.

1. Introduction

Floating offshore wind turbines (FOWTs) are reaching high technology readiness levels (TRL) and start operating at sea in commercial wind farms. They are expected to operate for several decades and must endure fatigue and extreme loadings induced by waves, current and wind. The design procedures consider 50 to over 100-year return period environmental conditions to dimension the support structure of these turbines. Uncertainty in state-of-the-art numerical models in such conditions logically can lead to costly conservative designs. In order to reduce the cost of offshore wind power, we thus need to improve our knowledge and understanding of the response of FOWTs in rough environmental conditions.

The dynamic response of bottom-fixed offshore wind turbines (OWTs) have been studied for some years, including hydro-elastic effects induced by extreme sea states where linearised theories do not apply. For simple geometries, theoretical models were developed to calculate high-order hydrodynamic loads [8, 19, 24], often assuming long-crested waves. Experiments were conducted in order to capture these hydro-elastic effects for monopile substructures, following several strategies. Some considered rigid structures mounted on a flexible joint to measure the mudline overturning moment [28, 19, 2]. The response of the experimental models in regular or extreme waves was studied, in order to validate theoretical and numerical models, particularly for the ringing response of monopiles. More recent experiments used an inner core structure (backbone) providing the desired stiffness and respecting Froude-scaled bending mode frequencies (at least on the first mode), on which an outer shell of the correct geometry was mounted in order to respect Froude-scaled hydrodynamic loads [4, 3]. These experiments contributed to validate numerical models developed to study nonlinear hydro-elastic response of such bottom-fixed OWTs [31, 21].

Concerning FOWTs, their responses to miscellaneous sea-states and with several types of floaters have firstly been studied using hydro-aero-elastic simulation tools [17, 26]. Many experimental campaigns have been completed following a similar modelling strategy, with a rigid platform and an elastic tower aiming at capturing the Froude-scaled first bending mode frequency [16, 27, 1]. The tower could also be kept rigid, for a matter of simplicity or to respect the aerodynamic effects induced by the tower [33, 34]. The elasticity of the substructure has been ignored in most of the analyses. The studies notably concluded that numerous simulation tools were able to simulate the response of such system in various environmental conditions, including the response of the first tower bending mode [27]. It was also observed that spar-type FOWTs may have larger tower base bending moments than tension leg platforms (TLP) or a semi-submersible FOWTs, mainly because of large inertial and gravity loads [18, 10].

FOWTs may also be subjected to steep sea-states, where high-order hydrodynamic loads could have an impact on the platform's response. Various environmental conditions may trigger structural vibration of the first or subsequent flexible modes [29]. Vibrations may be mostly triggered by aero-

*Corresponding author
vincent.leroy@ec-nantes.fr (V. Leroy)
ORCID(s):

dynamic loadings and aero-elastic couplings or by hydro-elastic couplings. The latter becomes crucial with the increasing sizes of the FOWTs and of their substructure, bringing the natural frequencies closer to hydrodynamic excitation frequencies. The hydro-elastic couplings concern a wide range of frequencies that need to be investigated. Ringing could occur in a very steep wave group, with or without impact, where many modes could be triggered, inducing extreme loads in the foundation or the hull. A steady-state springing response can happen under the excitation of high frequency hydrodynamic loads (typically sum-frequency second order loads) when they trigger a flexible mode of the structure [12].

Hydro-elastic couplings in OWT substructures have been the focus of recent numerical developments and analyses including structure deformation in potential flow theory [6, 11, 22, 30, 15, 21] or in Morison-based models [36, 35]. The studies conclude that such effects could be significant for large FOWTs. The nonlinear hydrodynamic loads and wave-structure interaction could also play an important role in severe sea states.

Few experiments have been completed to validate the numerical developments, particularly because of the difficulty in scaling the hydro-elastic effects and the incompatibility in the Froude-scaling of both the hydrodynamic loads and the structure response. A first approach is to measure the internal loads on a rigid structure or, more precisely, at a link between two rigid segments of a platform [23]. The internal bending moments can hence be measured but the deformation of the platform segments is then negligible and the full hydro-elastic couplings are not captured. Similarly, the internal loads and bending moments could for instance be experimentally assessed on a rigid segmented hull, using load cells between ship segments [14, 7]. Another tested strategy considers an inner skeleton providing the correct structure stiffness on which an outer shell is installed in order to correctly reproduce Froude-scaled hydrodynamic loads [32].

This study presents an experimental investigation of the hydro-elastic response of a spar-type 10 MW FOWT, with a platform based on an in-house design. A new Froude-scaled wind turbine model has been designed and built, with flexible tower and platform, along with a rotor-induced thrust force emulator based on a software-in-the-loop (SIL) approach. The design of the platform is made softer than existing floating wind turbines to anticipate the hydro-elastic couplings that would occur on systems larger than the actual ones. The substructure has been designed following the last strategy presented above: a inner skeleton provides the desired stiffness and an outer shell is subjected to Froude-scaled hydrodynamic loads. The first fore-aft bending mode frequency of the whole structure is Froude-scaled. Some of the hydro-elastic effects and the vibrations of the body at this frequency can hence be correctly reproduced at a scale 1:40.

The wind turbine model is studied in several conditions: regular waves of different periods and several steepnesses and various irregular waves conditions, with and without constant thrust force. The linear and nonlinear response of the structure is studied. Particularly, the bending resonance induced by 2nd or higher-order hydrodynamic loads is observed. In irregular waves, this can result in strong springing/ringing of the structure.

2. Experiments

2.1. Experimental set-up

2.1.1. Test model design

A wind turbine model has been designed for the sake of this experimental study. The objectives of the design are listed as follows:

- Respect the Froude similarity, at a scale 1:40, on both the hydrodynamic loads and the natural frequencies for rigid body motions (surge, sway, heave, roll, pitch and yaw);
- Respect the Froude similarity on the first fore-aft bending mode of a large FOWT of 10 MW rated power: the targeted frequency is 0.4 Hz at full scale [13];
- Measure the bending strain on the model and internal loads.

The higher-frequency modes are not at stake in the model design as they are too far from wave-induced hydrodynamic force frequencies to be relevant for a hydro-elastic analysis.

The chosen turbine is the DTU 10 MW turbine [5], supported by a spar platform designed at Centrale Nantes [1]. A CAD view of the whole model is shown in Figure 1. If not specified otherwise, all dimensions are given at full-scale in the following. The platform has 90 m draft, 18 m diameter below the taper and 11.2 m diameter at the waterline.

The modal frequencies depend on the bending stiffness and on the mass distribution. In order to scale down the bending stiffness of a beam, one should scale down EI_y, where E is the Young's modulus and I_y is the second moment of inertia of the beam's cross-section. To respect the Froude similarity on the first fore-aft bending mode frequency of the whole complex assembly, an iterative process has been completed between the model design and numerical modal analysis. The final design is composed of an inner backbone of aluminium (which has a low Young's modulus compared to steel, for instance) with a reduced diameter and thickness to reduce the bending stiffness. Light floaters are mounted around it to respect the outer geometry (and Froude-scaled hydrodynamic loads). The backbone has a diameter of 100 mm and a thickness of 5 mm.

Ballast is mounted at the bottom, and three pairs of light floaters are clamped at different locations of the backbone, on the squared sections visible in Figure 1.

A clearance is ensured between floaters and between the floaters and the backbone to avoid contact when the structure bends. The floaters are made of polyurethane. The main part of the spar is divided into three pairs of floaters to limit the number of fixation points on the backbone. A larger number of floaters would request a large number of melded sections,

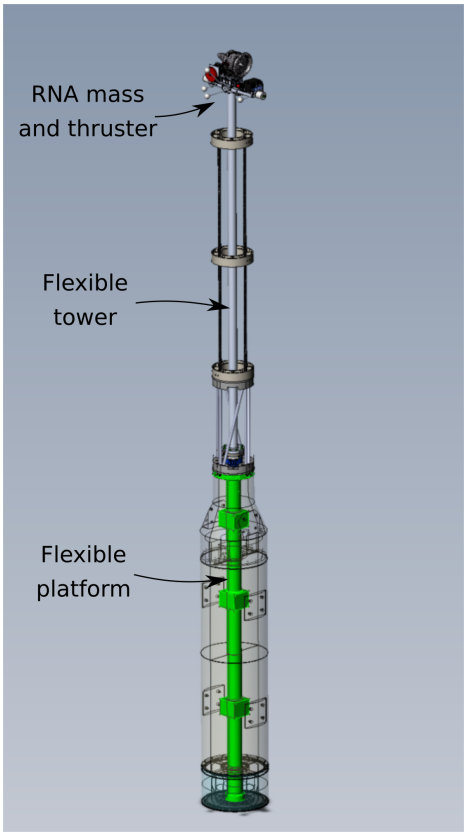

Figure 1: CAD view of the FOWT model. The platform inner backbone is highlighted in green and the floaters and ballast around it are made transparent. The flexible tower, the structure carrying the cables and the RNA are also visible on top of the platform.

which would alter the stress fields and the strain measurement on the beam. With the chosen assembly, the structure can freely bend and its response can be approximated with linear Euler-Bernoulli theory as discussed in Section 2.1.4. It is however difficult to estimate how much this coarse assembly affects the modes shapes.

The wind turbine, consisting of the tower and rotor-nacelle assembly (RNA), is mounted on top of the platform. A light carbon structure surrounding the tower is also visible in Figure 1, which is used to carry cables from the RNA to the connection point at the bottom of the tower, without altering the dynamics of the wind turbine. As previously mentionned, the RNA is inspired from the DTU 10 MW turbine: it has the same targeted mass and position of center of gravity. An actuator is used to represent the action of the wind and is presented later in Section 2.1.2.

The mass and geometry of the platform model is detailed in Table 1. The properties of the wind turbine are given in Table 2. Previous spar designs in the literature carrying the same wind turbine showed first fore-aft bending mode frequencies between 0.4 and 0.56 Hz [13, 1]. The design target for this model is 0.4 Hz (full scale). A soft design was chosen for two reasons: to anticipate the hydro-elastic couplings that would occur on larger than actual turbines, and to be able to accurately measure the strain on a model-scale platform for code validation purposes. The obtained frequency for the first bending mode of the assembled model is 0.39 Hz (full scale) as described in Section 2.2.

Figure 2 shows a photo of platform assembly (with one of the top floaters missing) and of the whole platform. Figure 2a also shows the strain gauges installed on the platform backbone, which are discussed in Section 2.1.4.

2.1.2. Rotor thrust force

An actuator is used to represent the aerodynamic thrust force. The RNA uses a single-rotor thruster, designed in the SoftWind project [1]. It is installed on the tower top and is shown in Figure 3.

In the SoftWind project [1], the applied aerodynamic thrust was calculated in real-time in a *Software-In-the-Loop* (SIL) framework. In this study, only a constant thrust is applied. The reason for this is the simplification of the aerodynamic load for an analysis focused on the hydro-elastic response. The constant thrust gives a positive tilt of the platform, and enables investigating its effect on the wave-induced response, but the aero-hydro-elastic couplings are not studied in these experiments.

2.1.3. Installation and mooring

The FWT model is installed in the Ocean Engineering and Hydrodynamic wave tank of Ecole Centrale Nantes in France. The wave tank is 50 m long, 30 m wide and 5 m deep. 48 flap-type wave-makers are on one side of the wave tank and an absorbing beach is at the other end to avoid wave reflection. The waves propagate along the positive x direction.

A linear aerial mooring system is used. The reason for this is mainly to simplify the calibration of an equivalent numerical model. The focus of the present study is primarily the wave-induced structural loads. In the perspective of code validation, it is interesting to be able to represent the mooring loads using a simple linear restoring force and to avoid hydrodynamic loads on the lines or nonlinear mooring restoring forces. Additionally, most of the analysis in this paper is made without aerodynamic loads. The effects of nonlinear mooring loads might thus play a limited role in the overall dynamics of the system.

A bird's eye view of the mooring layout is shown in Figure 4a. Each mooring line is composed of an inextensible string and a spring of linear stiffness. A photograph of the mooring fairleads is displayed in Figure 4b, showing also the load cells installed on each line. The springs are installed at the other end, on the wave tank walls. The calculated global resulting stiffness (full-scale) for the whole mooring system is:

- 121.3 kN/m in the x direction (or wave heading);
- 97.3 kN/m in the y (transverse) direction.

Table 1
Geometry and mass properties of the platform model (full scale).

draft	90	m
diameter below tapper	18	m
diameter at waterline	11.2	m
Platform height above waterline	4	m
Platform mass	1.88E+07	kg
Platform COG w.r.t waterline	-71.6	m
Platform pitch inertia at its center of gravity	5.46E+09	kg.m^2

Table 2
Geometry and mass properties of the wind turbine (full scale).

Wind turbine rated power	10	MW
Hub height	119	m
Height of WT COG above waterline	53.117	m
WT mass	$2.11E+06$	kg
Iyy of the WT around its COG	$4.73E+09$	kg.m^2

2.1.4. Sensors

First, the wave elevation is measured using resistive wave gauges. Five gauges are installed in the wave tank as described in Figure 4a. At y=-7.5 m, following the reference frame of Figure 4a, 4 gauges are installed in line with a spacing of 40 cm in order to have several measurement of the wave elevation in the main wave heading. Another gauge is installed at y=7.5 m at the equilibrium position of the model in the x direction (at x=0). This last measurement is redundant for unidirectional waves.

Several other sensors are also used to measure the response of the FWT model. The motion of the model is mea-

(a) Spar top before the last floater was mounted. The strain gauges are visible on the aluminium backbone.

(b) Full platform model when it was first put into the water.

Figure 2: Photos of the assembly of the spar platform model.

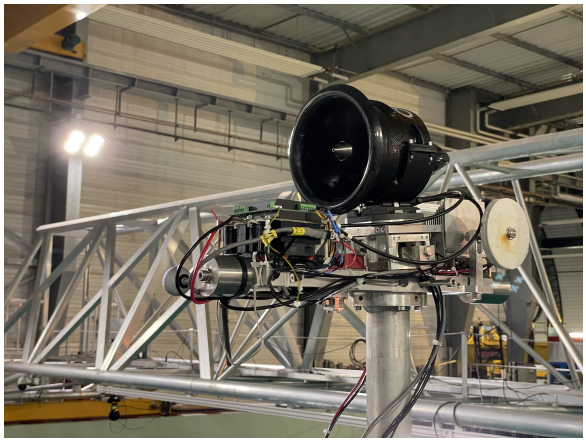

Figure 3: Photo of the RNA. The thruster is visible in black. Masses are added to adjust the position of the COG.

sured using a Qualysis motion tracking system. The position (6 degrees of freedom) of two sections is measured: the tower top and the platform top. The rotations (pitch and roll) of the platform bottom are also measured using an inertial measurement unit (IMU). Accelerations are measured using tri-axial accelerometers on the RNA, at the platform top and at the platform bottom.

Concerning forces, the internal loads are measured between the platform and the wind turbine tower, at what shall be called the transition piece (TP) on a full-scale FOWT. The full generalised load vector is measured, including three forces and three moments around three axes x, y and z. The aerodynamic load induced by the RNA thruster is measured using a 2-axis load cell, installed between the nacelle and the thruster. The inertial and weight loads are removed from this force measurement, using the measured accelerations, in order to extract the thrust force. The mooring line tension at the fairlead is also measured in each of the four lines.

As mentioned in Section 2.1.1, the outer floaters are mounted with a sufficient clearance between them and the backbone to allow free bending of the spar platform. The strain of the platform is then measured using strain gauges installed on the aluminium backbone at three locations: at $z_1 = 90$ m, $z_2 = 73.48$ m and $z_3 = 62.44$ m from the spar bottom (z_1 is at the waterline).

Full Wheatstone bridges of strain gauges are installed on the aluminium tube. Assuming that the backbone behaves following Euler-Bernoulli beam theory, it is possible to determine an equivalent bending strain value, obtained from the measurement of the antisymmetric strain over the beam's cross-section. This approach requires the gauges to be installed far enough from any weld bed, which would alter the stress field in the material. The full bridge can provide a measurement in $\mu m/m$ and also has the advantages of being more accurate than a regular strain gauge because is cancels the effect of the cables resistance.

These gauges allow the measurement of the strain induced by the bending around the pitch and roll axes. The bending strains measured around the pitch axis are respectively called $\epsilon 1$, $\epsilon 2$ and $\epsilon 3$. The strain gauges are located where the strain is expected to be large (near the top of the spar), and far enough from any weld bead, to avoid alteration in the stress field.

As mentioned before, Figure 2a shows a photo of the top section of the platform model, before the last floater was mounted. Two pairs of strain gauges are visible on the aluminium tube (at z_1 and z_2). The section where the top pair of floaters is clamped is visible, as well as the clearance between the floaters and the backbone. The backbone was first tested alone in a cantilever beam configuration to ensure that the strain matched theoretical models and that the welded square sections had little impact on the strain. The measured strain had a very good agreement with the Euler-Bernoulli beam theory (below 2% relative difference). A summary of the sensors installed on the platform model is presented in Figure 5a.

Cables transmitting the sensor signals and the electrical power for the thruster were installed between the model and a footbridge over the water, in the form of two garlands, one on each side of the model. The garlands were installed in the direction transverse to the wave heading in order to limit the impact on the system's dynamics. Figure 5b shows a picture of the model installed in the wave tank with the two garlands of cables. All cables are connected to sensors in the white box visible in the figure. The analysis of the motions of the model in decay tests, performed with and without the garlands, showed that the garland have a negligible impact on the model dynamics.

2.1.5. Repeatability

It is very difficult to account for every source of uncertainty in such experiments. Repeatability tests are hence performed in order to ensure the consistency of the measurements. An irregular sea state condition, defined by a JONSWAP spectrum with a significant wave height $H_s = 4$ m, a peak period $T_p = 10$ s and a peak enhancement factor $\gamma = 3.3$, with a constant thrust of 1 MN on the thruster (67 % of the nominal thrust), was run 11 times. The environmental conditions and the measurements are given at full scale. A standard Froude scaling law is used for the extrapolation. A time window of the wave elevation, accelerations, forces and strain measurements is shown in Figure 6. The repeatability is very good. All the strain measurements in this repeatability test have a cross-correlation above 97 % with the mean value of all signals, chosen as reference. Similarly, for this run, the waves signals have a cross-correlation of above 96 % with the mean reference waves measurement. This gives good confidence in the precision of the measurements made on the model.

2.2. Characterization of the model

Decay tests are performed to identify the natural periods of the rigid degrees of freedom. The current model is studied for unidirectional waves, propagating along the x axis. The most important rigid degrees of freedom are hence the surge, heave and pitch. Their respective natural periods are 128 s,

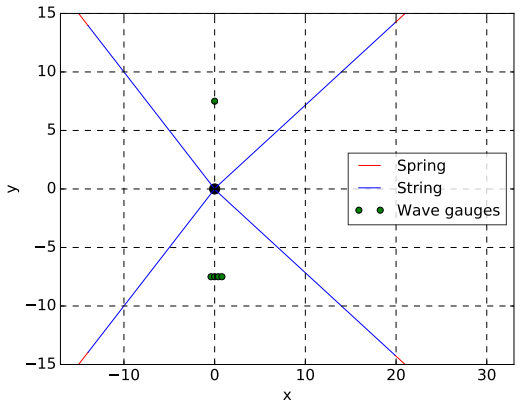

(a) Bird's eye view of the mooring layout. Positions of the anchoring points are given at the model scale.

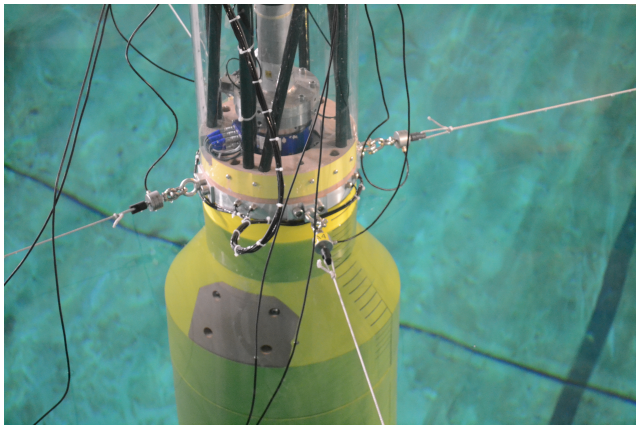

(b) Photo of the mooring fairleads on the model.

Figure 4: Mooring system for the model in the wave tank.

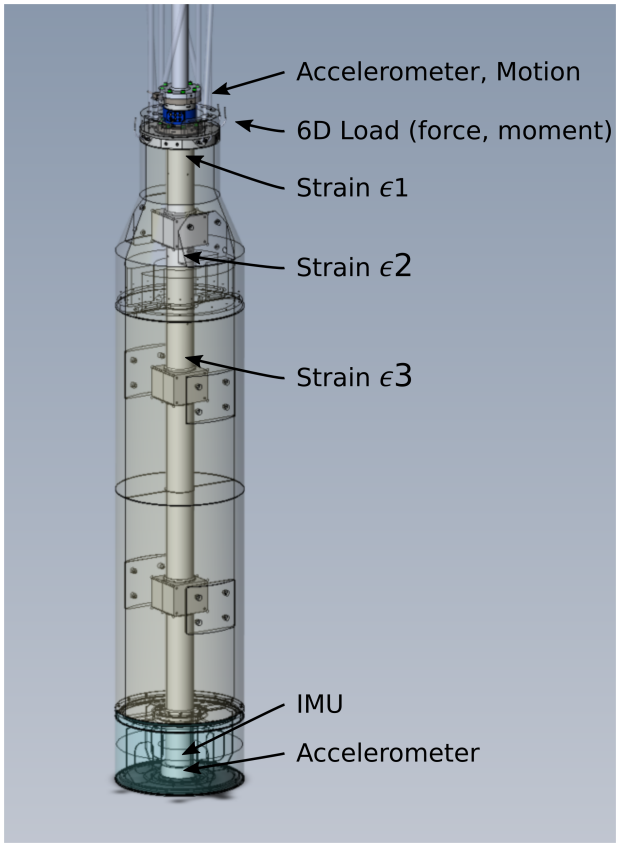

(a) Summary of the sensors installed on the spar model.

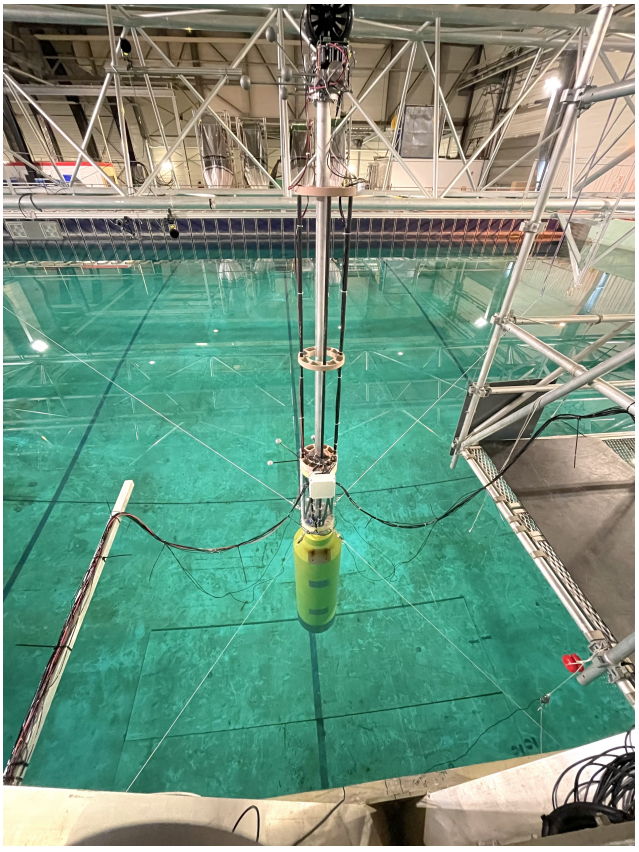

(b) Installation of the model in the wave tank, with the cables garlands visible on both sides of the model. The wave-makers are visible in the background.

Figure 5: Spar model: sensors and cables.

30.7 s and 33.7 s. During the experiment, the sway, roll and yaw were negligible.

Hammer tests are done to identify the flexible mode frequencies. A hammer hits the wind turbine model at different locations: on the nacelle and slightly above the tower base, to make sure several modes are excited. Hammer tests are also done in the transverse direction (along the y axis) to identify possible couplings between the fore-aft and side-side bending modes. The accelerations measured at several positions (nacelle, tower base and platform bottom) are analysed in frequency domain. A spectrum of the accelerations measured on the nacelle, obtained after a hammer impact on the

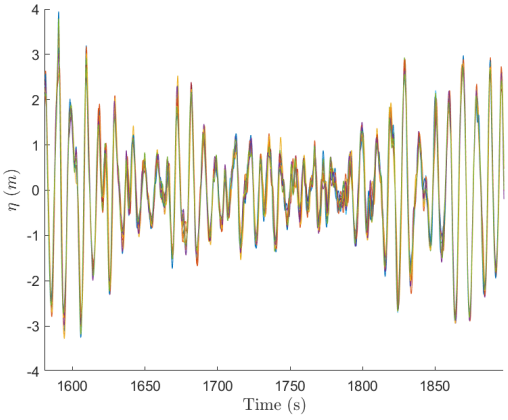

(a) Free surface elevation for the repeatability test.

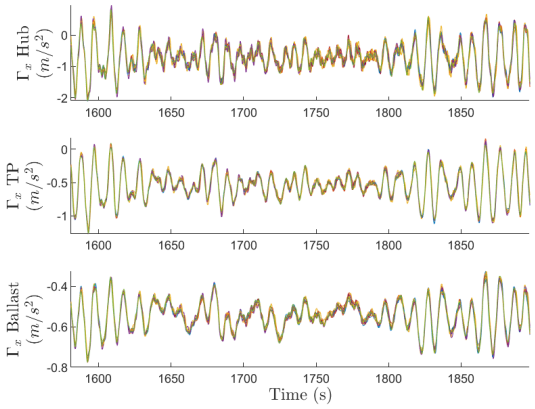

(b) Accelerations on the X axis, at the nacelle, at the transition piece (TP) and at the spar ballast.

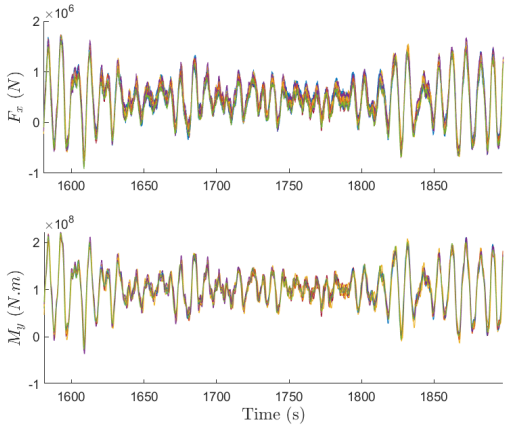

(c) Force on the X axis and bending moment at the transition piece (TP).

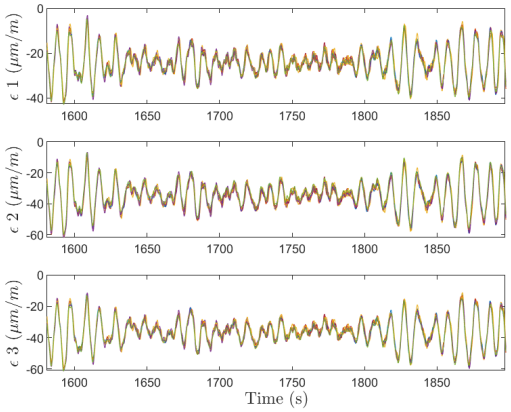

(d) Strain on the spar platform.

Figure 6: Repeatability test in irregular waves.

Table 3
Natural periods of the model.

Degree of freedom	Natural period
Surge	128 s
Heave	30.7 s
Pitch	33.7 s
1st bending mode	2.58 s

tower base, is plotted in Figure 7. The hammer impact is not perfectly aligned in the x or y direction and excites both the fore-aft and side-side bending modes each time. The first bending modes (fore-aft and side-side) are both located at 0.39 Hz (full scale). The second bending modes are observed at around 1.42 Hz and the third bending modes at 2.92 Hz. The pitch and roll natural frequencies can be observed at around 0.03 Hz, at much lower frequencies. Similar observations can be made by analysing the strain spectra, for instance. The response of the higher modes will not be analysed in the study. The results natural periods are summarized in Table 3.

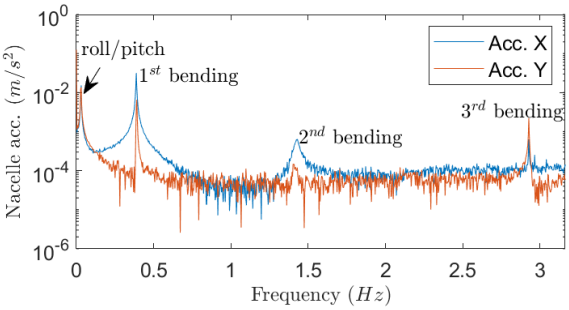

Figure 7: Nacelle accelerations spectra after an impact on the tower base, in the x direction. Accelerations on x and y-axes are plotted.

The decay of the first fore-aft bending mode is then studied by filtering measured accelerations with a band-pass filter, focused on the mode frequency. The signal is studied in time domain in order to estimate the structural damping on this mode. The decaying acceleration after a hammer impact on the nacelle in the x-direction is plotted in Figure 8. An

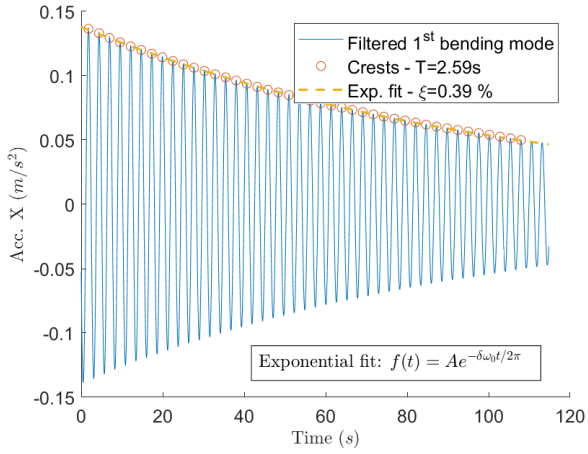

Figure 8: Decay of the acceleration on the nacelle after a hammer test.

exponential fit is applied to the decaying acceleration's envelop $f(t)$. The exponent of the exponential is linked to the damping in still water ξ with the relation: $f(t) = A_0 e^{-\xi\omega_0 t}$, where A_0 is the amplitude at the start of the response and ω_0 is the natural frequency. The damping is thus estimated at 0.39 %.

2.3. Environmental conditions

The FOWT has been studied in various environmental conditions:

- Regular waves, with periods ranging from 4.9 to 19 s and steepnesses of $\frac{H}{\lambda} = 2$, 4 and 6 %;
- Irregular sea states, of various significant wave heights H_s and peak periods T_p, inspired from the Gulf of Maine site [9] and detailed later.

The response of the model has been studied with and without wind thrust:

- The regular waves have been studied without thrust, and with 50 % and 67 % of the nominal wind thrust (800 kN and 1000 kN respectively);
- The irregular sea states have been studied without thrust, and with a constant thrust defined by the mean value of the thrust obtained with a probable wind speed at the chosen (H_s,T_p) conditions.

The regular waves are described in Table 4, for each wave period and steepness. The two last waves with 6 % steepness could not be ran because of measurement limitations. One can see the wave periods 5.20 s, 7.75 s and 10.33 s are respectively 2, 3 and 4 times the 1st fore-aft bending mode period. High-order hydrodynamic loads are hence expected to trigger the bending resonance of the structure. The regular waves generated in the wave tank are compared with a reference wave, calculated with a fully nonlinear Rienecker-Fenton model [25] as shown in Figure 9, for example. The

Table 4
Tested regular waves (full scale), for each wave period and steepness. The periods matching 2, 3 and 4 times the 1st fore-aft bending mode period are highlighted in bold.

T (s)	H - 2% (m)	H - 6% (m)	H - 6% (m)
4.93	0.76	1.52	2.27
5.20	0.84	1.69	2.53
5.45	0.93	1.85	2.78
6.73	1.41	2.83	4.24
7.75	1.87	3.75	5.62
8.26	2.13	4.26	6.39
9.79	2.99	5.99	8.98
10.33	3.33	6.66	9.99
11.32	4.00	8.00	12.00
12.85	5.16	10.31	15.47
14.38	6.45	12.90	19.36
15.91	7.88	15.76	23.63
17.44	9.41	18.81	-
18.97	11.01	22.01	-

Table 5
Irregular sea states considered for the wind turbine model (full scale).

No.	Tp (s)	Hs (m)	F (kN)
1	5.0	3.0	1000
2	6.0	1.5	1500
3	6.5	1.5	800
4	8.0	3.0	1500
5	10.0	4.0	1000
6	13.4	8.9	570
7	13.8	9.4	300
8	13.8	10.9	400

two plotted waves are the aforementioned $T = 7.75$ s and 10.33 s waves with a steepness of 4 %. The agreement is very satisfactory.

The irregular sea states (SS) are described by their H_s and T_p, given in Table 5. The three last conditions correspond to the 5-year, 10-year and 50-year return period sea-states, respectively. The aerodynamic thrust, chosen as a function of a wind speed correlated with each sea-state, is also given in the table. The response of the model is studied for around 2 hours (full scale) in each run, with three sets of wave phases. As an example, two measured wave spectra are compared to the targeted JONSWAP spectra in Figure 10. The amplitude at the peak appears overestimated, but the relative differences between the measured and targeted significant height H_s are respectively 0.9 % and 1.9 %, which is satisfactory.

3. Results and discussion

3.1. Response in regular waves

As presented in Section 2.3, the model has been tested in a series of regular waves, with increasing steepness $\frac{H}{\lambda} =$ 2 %, 4 % and 6 %. For the two first values of wave steepness, the wave periods range from 4.93 s to 18.97 s and wave the heights from 0.76 m for the smallest to 23.63 m for the high-

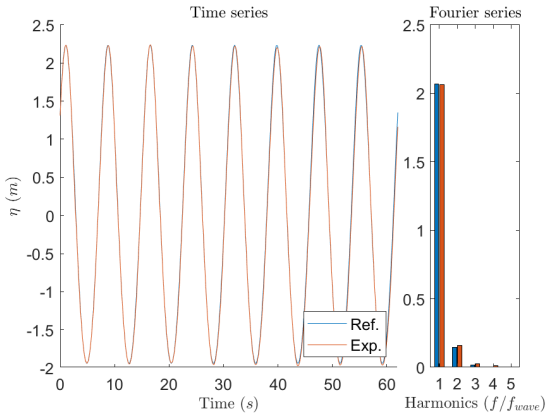

(a) $T = 7.75$ s, $H = 4.18$ m, $\frac{H}{\lambda} = 4$.

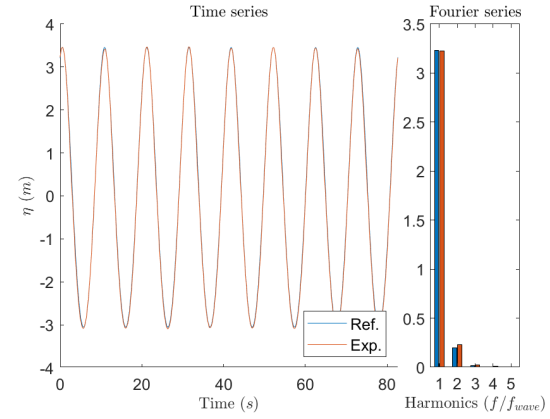

(b) $T = 10.33$ s, $H = 6.61$ m, $\frac{H}{\lambda} = 4$.

Figure 9: Example of theoretical (Rienecker-Fenton) and measured regular waves.

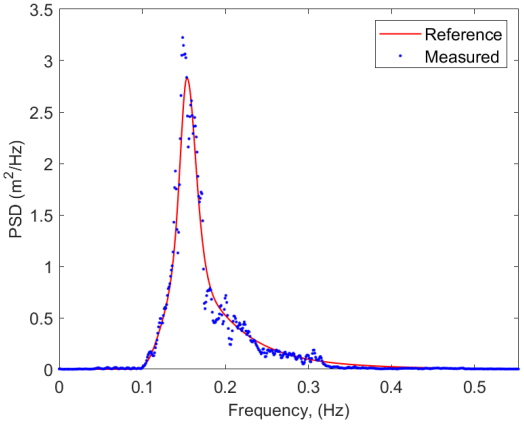

(a) $H_s = 1.5$ m, $T_p = 6.5$ s.

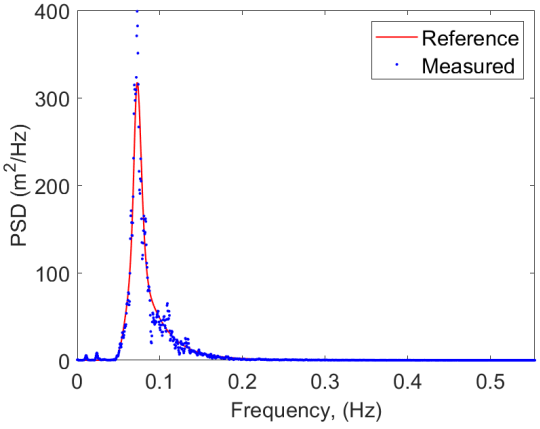

(b) $H_s = 10.9$ m, $T_p = 13.8$ s.

Figure 10: Example of theoretical (JONSWAP) and measured irregular waves spectra.

est and steepest wave. Concerning wave models, the correct wave model to describe the regular waves would be at least the Stokes 2nd order model for the 2 and 4 % steepness waves, and at least the Stokes 3rd order model for the 6 % steepness waves [20].

The response of the model is studied for the time period before the reflected wave comes from the beach. The usable time depends on the wave periods and ranges from 2 wave periods for the longest to over 20 periods for the shortest wave period. First, the first order response to the wave excitation is studied and the response amplitude operators (RAOs) are computed. The surge, heave and pitch RAO of the system are plotted in Figure 11a, and the RAOs of the strain along the platform's backbone are plotted in Figure 11b. $\epsilon 1$ is the strain measured at the platform top, $\epsilon 2$ and $\epsilon 3$ are lower along the platform, as detailed in Section 2.1.4. The RAOs are calculated for regular wave tests, with and without an aerodynamic constant thrust equal to 67 % of the rated thrust (i.e. 1000 kN). The cases with wind thrust are indicated with a "T" in Figure 11a. The RAOs are calculated based on a Fourier analysis: they are equal to the harmonic of the measurement at the wave frequency divided by the measured wave's first order amplitude.

The studied wave periods range from 5 to 19 s, all of which are below the rigid modes' periods. The observed motion RAOs are then as expected, with amplitudes increasing with the wave periods.

At frequencies far below the natural frequencies in bending, the bending of the platform is the sum of two contributions: the inertia loads, due to the motion and rotation of the model, and the quasi-static bending induced by the weight of the wind turbine and the pitch angle of the platform. The former decreases and the latter increases as the wave period increases. This explains the shape of the bending strain RAOs, with a maximum observed at around 8.3 s for $\epsilon 2$.

The constant thrust has no effect on the first order amplitude of the response. The wave steepness does not have an impact either, as only the linear response is extracted in this analysis.

However, the model shows a highly nonlinear response at several wave periods. In particular, a resonant response of the 1st fore-aft bending mode was observed at 3 wave periods: 5.2 s, 7.75 s and 10.33 s. For instance the strain time series obtained at the steepest case (i.e. 6 %) when the wave

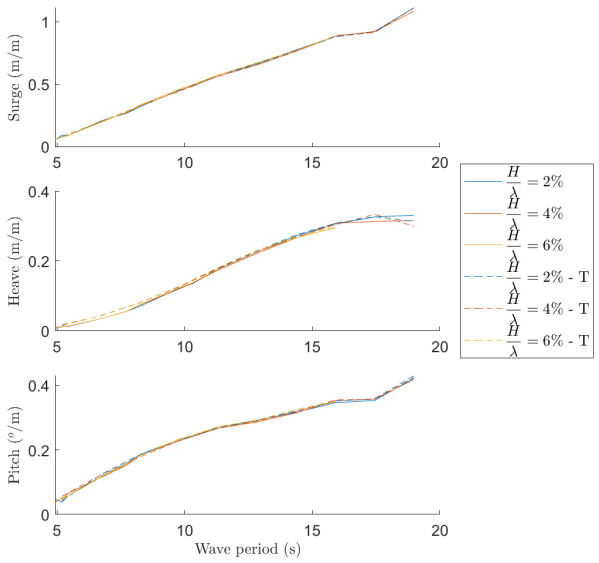

(a) Motion RAOs.

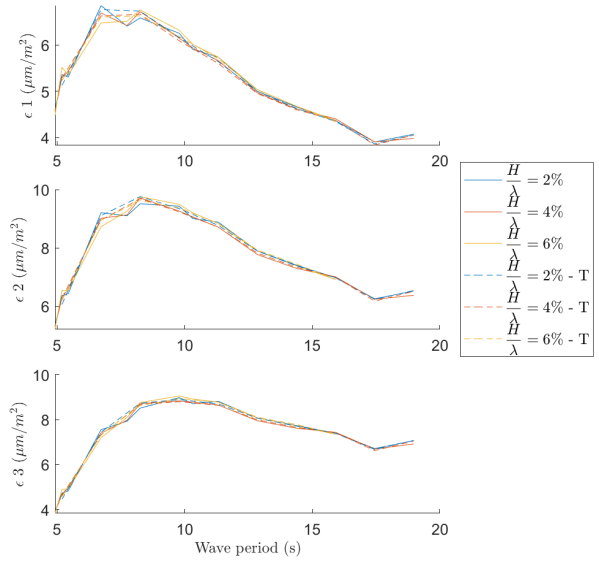

(b) RAOs of the strain along the platform's backbone.

Figure 11: RAOs obtained in regular waves for 3 different wave steepnesses with and without constant thrust force. The runs with rotor thrust are indicated with the letter T in the legend.

periods equals twice the 1st bending mode period is plotted in Figure 12. This plot shows the transient response, and it does not reach a steady-state.

A sliding harmonic analysis is used to study the frequency content of the response. The n-th Fourier series coefficient of a function f can be calculated on a one-wave period moving window as written in the following equation [7].

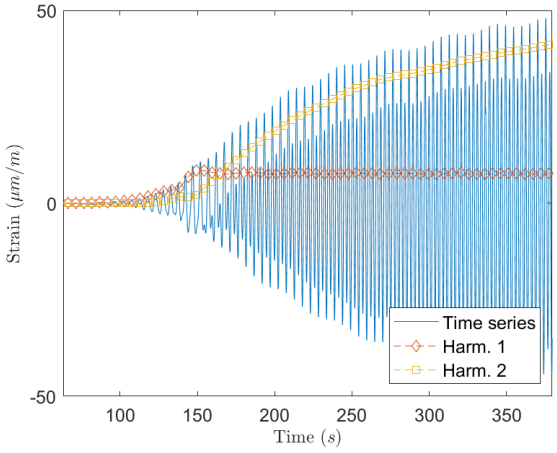

Figure 12: Bending strain ($\epsilon 2$) time series (including transient) at $T = 5.2$ s and with $\frac{H}{\lambda} = 6$ %.

$$c_n(t, \omega, f) = \frac{1}{T} \int_{t-\frac{T}{2}}^{t+\frac{T}{2}} f(\tau)\, e^{-in\omega\tau}\, d\tau \tag{1}$$

This moving harmonic analysis is performed to calculate the first five harmonics of the strain, for instance, with one window per wave period. The first and second harmonics of the strain are plotted in Figure 12. The first harmonic reaches a steady state after only a few oscillations, but the second harmonic keeps increasing until the end of the measurement. This increase is due to the resonance of the 1st bending mode, excited by the second order hydrodynamic loads, and the small structural damping. In the case where the excitation is large enough to increase the resonant response, the system cannot reach a steady state. The results of the harmonic analysis in the following may then be underestimated when T=5.2 s.

The strain at several periods with $\frac{H}{\lambda} = 6$ % is plotted in Figure 13. The first and second harmonics on each wave period (computed with a sliding harmonic analysis) are plotted too. The five first harmonics, computed on the total analysis window, are also plotted on the right hand side of the Figure for each chosen wave. The resonance of the 1st bending mode (at the eigen period $T_{ben} = 2.58$ s) is triggered at the wave periods of $T = 2T_{ben} = 5.2$ s, $T = 3T_{ben} = 7.75$ s, and $T = 4T_{ben} = 10.33$ s, by the 2nd, 3rd and 4th order hydrodynamic loads, respectively. Here the harmonics at the bending mode frequency reach 455 %, 51.5 % and 14.4 % of the 1st harmonic response for each wave aforementioned period. For the case $T = 2T_{ben} = 5.2$ s, the true steady state harmonic amplitude is not completely reached (see Figure 12) and is here underestimated.

The harmonic analysis of the measurements obtained at the three wave steepnesses and the three resonant wave periods are given in Figure 14. Even in the less steep cases, the responses of second and third harmonics for the wave periods of $T = 5.2$ s and 7.75 s, are substantial and respectively

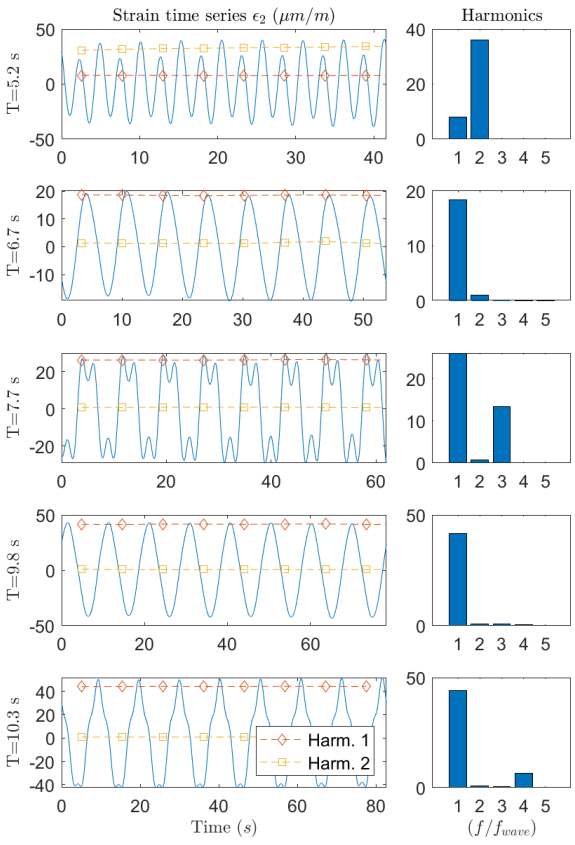

Figure 13: Steady-state strain ($\epsilon 2$) in regular waves at T = 5.2 s, 6.7 s, 7.75 s, 9.8 s and 10.33 s with $\frac{H}{\lambda} = 6$ %.

reach around 120 % and 10 % of the first harmonic. The second harmonic becomes larger than the first when the bending mode is excited by the second order wave. When the wave steepness increases, the nonlinear response increases greatly. Up to fourth order effects are visible in the steepest cases, at the bottom right-hand corner, where the fourth harmonic amplitude is 14% of the first.

3.2. Response in irregular waves

The response of the model is now studied in irregular waves. The irregular wave conditions were given in Section 2.3. Three sea states are selected for this analysis: SS 2, SS 4 and SS 8, respectively (H_s = 1.5 m, T_p = 6.0 s), (H_s = 3 m, T_p = 8 s) and the 50-year return period sea-state (H_s = 10.9 m, T_p = 13.8 s). The measured waves and strain spectra are plotted in Figure 15. No thrust on the nacelle is considered for these runs. The steepness of the three selected sea-states is approximately $\frac{H_s}{\lambda_p} = 3$ %. The spectra are calculated on a window of around 2 hours (full scale), which does not include the transient regime at the wave-maker start. The transverse basin modes have a negligible effect on the results because the waves are mono-directional, and most modes are above the studied frequencies.

The strain spectra show a large response at the wave frequencies, ranging from 0.05 Hz to 0.3 Hz in all presented sea states. The low frequency response at the rigid modes frequencies is also visible. This highlights nonlinear hydrodynamic loads, inducing low-frequency oscillations of the wind turbine platform. These oscillations are particularly visible for the first case (H_s = 1.5 m, T_p = 5.5 s), for which the response at the wave frequency is relatively small. For the strongest sea state, the wave frequency response is the strongest. In the three cases, a response at the 1st fore-aft bending mode frequency (0.39 Hz) is also observed.

The vibration of the 1st bending mode is induced by high frequency nonlinear hydrodynamic loads. In SS 1, the sum-frequency second order loads could induce these oscillations. For the other sea-states, with longer peak periods, the oscillating response of the wind turbine may be caused by even higher order effects. Considering code validation, this data would be relevant for comparison with fully nonlinear potential flow solvers (as long as the waves do not break and the viscous loads remain small) or high fidelity tools such as Computational Fluid Dynamics software, coupled with structure dynamics solvers. A Morison-type model, combined with wave kinematics from a fully nonlinear potential flow solver, may also be able to capture higher order effects.

Similarly to the regular wave analysis in Section 3.1, one can see that the $\epsilon 2$ bending strain is still larger than the two other measurements.

In the most severe sea-states, a few wave impacts near the top of the platform were also observed. Several times, springing/ringing events triggered by steep wave groups or even wave impacts were captured in these extreme sea states. By definition, the springing of a structure is a steady-state oscillation at the resonance frequency, triggered and maintained by nonlinear hydrodynamic loads. The ringing response is the damped oscillations at the natural frequency triggered by strongly nonlinear hydrodynamic loads induced by the passage of a steep wave group or a wave impact. But springing and ringing may in fact be difficult to distinguish: the steady-state springing response could be triggered and maintained if the waves steepness is large, and if high-order hydrodynamic loads frequencies match the bending mode frequency, but the ringing response of the structure could be also sustained by a sequence of several steep wave packets.

In order to study the effect of structure resonance in springing/ringing response of the turbine, the following time domain analysis focuses on:

- The free surface elevation, to identify steep wave groups;
- The bending strain $\epsilon 2$;
- The acceleration of the TP in the x-direction (just above the platform top).

The bending strain and the acceleration are plotted as raw and band-pass filtered around the natural frequency in order to identify the resonance of the 1st bending mode.

Several resonance events have been identified in the irregular wave cases. To investigate four of these responses in

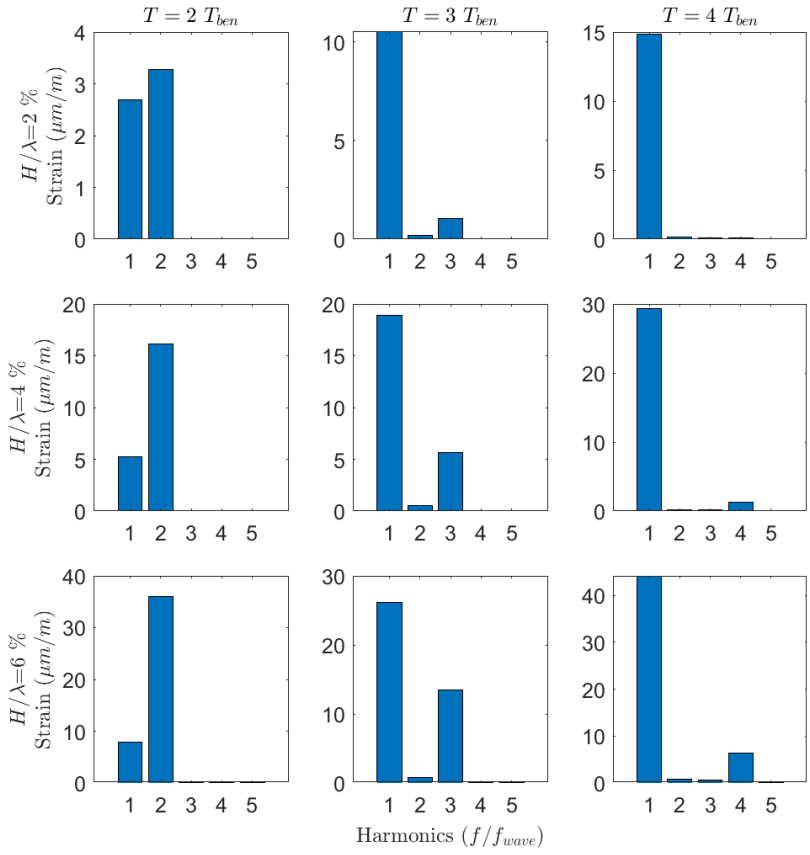

Figure 14: Harmonic analysis of the platform strain ($\epsilon 2$) in regular waves for waves periods of $T = 5.2$ s, 7.75 s and 10.33 s with $\frac{H}{\lambda} = 2$ %, 4 % and 6 %.

time domain, the free-surface elevation is plotted alongside the acceleration at the TP and the measured strains in Figure 16. The same wave conditions as before (SS 2, 4 and 8) are selected, at a chosen time window.

The weakest sea-state is studied in Figure 16a, and one can easily observe the growing bending mode response starting from 5150 s. No large acceleration peak is measured. The bending mode response is induced by a group of steep waves, and the first bending mode oscillation keeps increasing, being sometimes the main contribution to the strain. This bending resonant response is induced by oscillating high order hydrodynamic loads. In this case, according to the wave spectrum in Figure 15, sum-frequency second order loads should be the origin of this resonance response.

An intermediate sea-state (SS 4) is plotted in Figure 16b, with $H_s = 3$ m and $T_p = 8$ s. The bending response at the 1st bending mode frequency keeps increasing until around 4700 s as the waves increase. After this, the vibration is progressively damped, but the oscillation stays visible in the acceleration and strain measurements.

In the previously discussed sea states (SS 2 and SS 4), the total amplitude of the strain is however not very large. Given the design of the experimental model, described in Section 2.1.1, the amplitude of the strain may not be representative compared to that of a real full-scale wind turbine platform as only the resonant response was targeted in the design.

In the most severe sea-state SS 8 (50-year return period, with $H_s = 10.9$ m and $T_p = 13.8$ s) represented in Figures 16c and 16d, the response is of much larger amplitude. Similarly to the previous analysis, one can see that large wave groups trigger the 1st bending mode. In the two examples, the bending resonance keeps increasing incrementally, and each increase can be associated with a higher crest passing at the model's position. Steeper wave packets are observed at around 2435 s in Figure 16c and at around 980 s and 1060 s in Figure 16d. The transient effect can be an increase of the mode response which is then damped out after the excitation as in Figure 16d, or the induced additional oscillations can also happen with a phase shift with the already existing response, and hence result in a reduction of the springing response. In both cases, the springing and ringing oscillations are clearly visible in both the strain and the acceleration.

According to the wave and response spectra given in Figure 15, the resonance of the wind turbine model should here be induced by highly nonlinear hydrodynamic loads. Such wave loads may be possible in very steep conditions as dis-

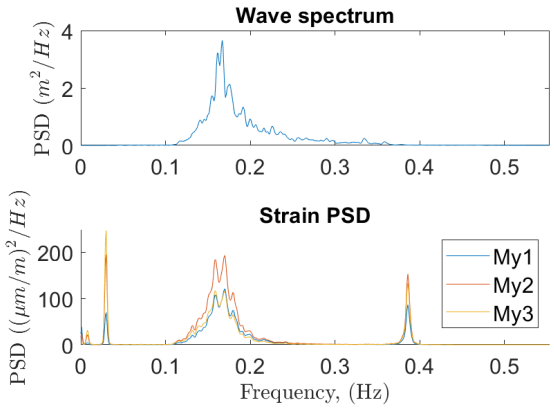

(a) SS 2: $H_s = 1.5$ m, $T_p = 5.5$ s.

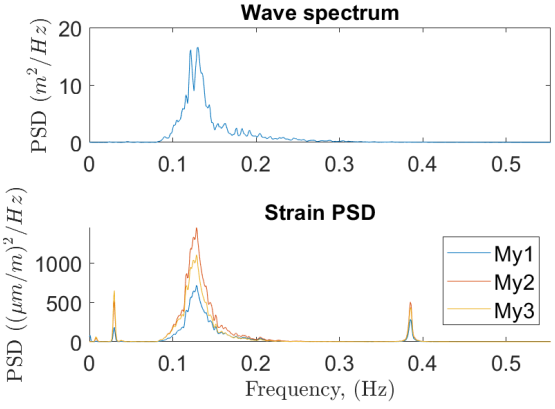

(b) SS 4: $H_s = 3$ m, $T_p = 8$ s.

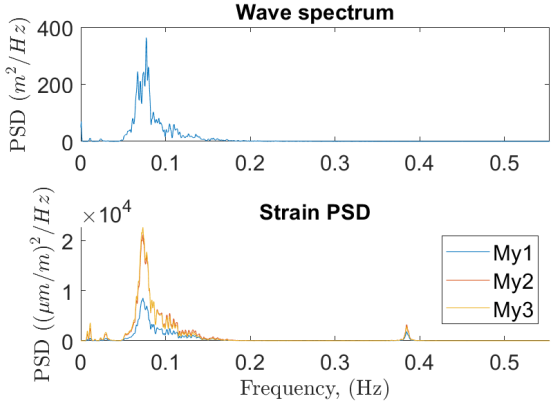

(c) SS 8: $H_s = 10.9$ m, $T_p = 13.8$ s.

Figure 15: Measured wave spectrum and strain spectra in several sea states.

cussed previously. More investigation may be necessary, on a more realistic wind turbine model, to evaluate if this can be critical for design. However, the presented measurements can be a relevant validation database of coupled simulation tools including nonlinear hydrodynamics and structure dynamics.

Wave impacts were also observed, particularly in the extreme conditions. An example is shown in Figure 17, with a large wave, inducing a significant and violent change in acceleration on the TP. This results in a large oscillation of the bending mode, which is damped in less than 200 s. The ringing responses observed before lasted for longer, sometimes for over 400 s.

4. Conclusion

A new experimental Floating Wind Turbine model has been designed to analyse the hydro-elastic response of its platform and tower. The platform is an in-house spar design, carrying the DTU 10 MW wind turbine, at scale 1:40. The main objectives of the design are to respect the Froude scaling of the hydrodynamic loads, natural frequencies on the rigid degrees of freedom, and the frequency of the 1st fore-aft bending mode. The model is thus made of a backbone, providing the correct elasticity, and relatively light floaters clamped onto it to respect the scaling of the geometry and hydrodynamic loads. Several measurements (accelerations, strains, and bending moment) allow an accurate monitoring of the hydro-elastic response of the wind turbine, additionally to motions and forces. Hammer tests confirmed the targeted bending mode period at around $T_{ben} = 2.58$ s. The chosen design was made softer than an existing FWT for two reasons: to anticipate the hydro-elastic couplings that would occur on larger than actual turbines, and to be able to accurately measure the strain on a model-scale platform, for code validation purposes.

The response of the model is first studied in regular waves, of different periods and three waves steepness: $\frac{H}{\lambda} = 2$ %, 4 % and 6 %. Amongst other wave periods, three wave periods are particularly relevant: the ones matching $T = 2T_{ben}$, $3T_{ben}$ or $4T_{ben}$. Then, the second, third or fourth hydrodynamic force harmonic respectively match the mode frequency, which triggers the resonance of the bending mode. High-order effects were observed, even in the smallest steepness $\frac{H}{\lambda} = 2$ %, where the bending strain of the backbone at the bending mode frequency was larger than the wave frequency response with $T = 2T_{ben}$. With the same steepness, when $T = 3T_{ben}$, the model response's 3rd harmonic is around 10 % of the 1st harmonic. This highlights the importance of nonlinear hydrodynamic loads in hydro-elastic couplings of such systems. Up to 4th order hydro-elastic effects were observed in the steepest waves. Outside these particular wave frequencies, the nonlinear response remained low in regular waves.

The model has then been studied in irregular waves, including short and steep sea-states, as well as extreme sea-states with return periods of 5, 10 and 50 years, all inspired by the Gulf of Maine site [9]. The analysis of the strain response in the platform backbone showed resonance responses of the model induced by strongly nonlinear hydrodynamic loads, including springing and ringing responses in steep waves conditions. This has been highlighted with several examples in various sea-states. For example, the short sea-states induced strong resonance of the bending mode, prob-

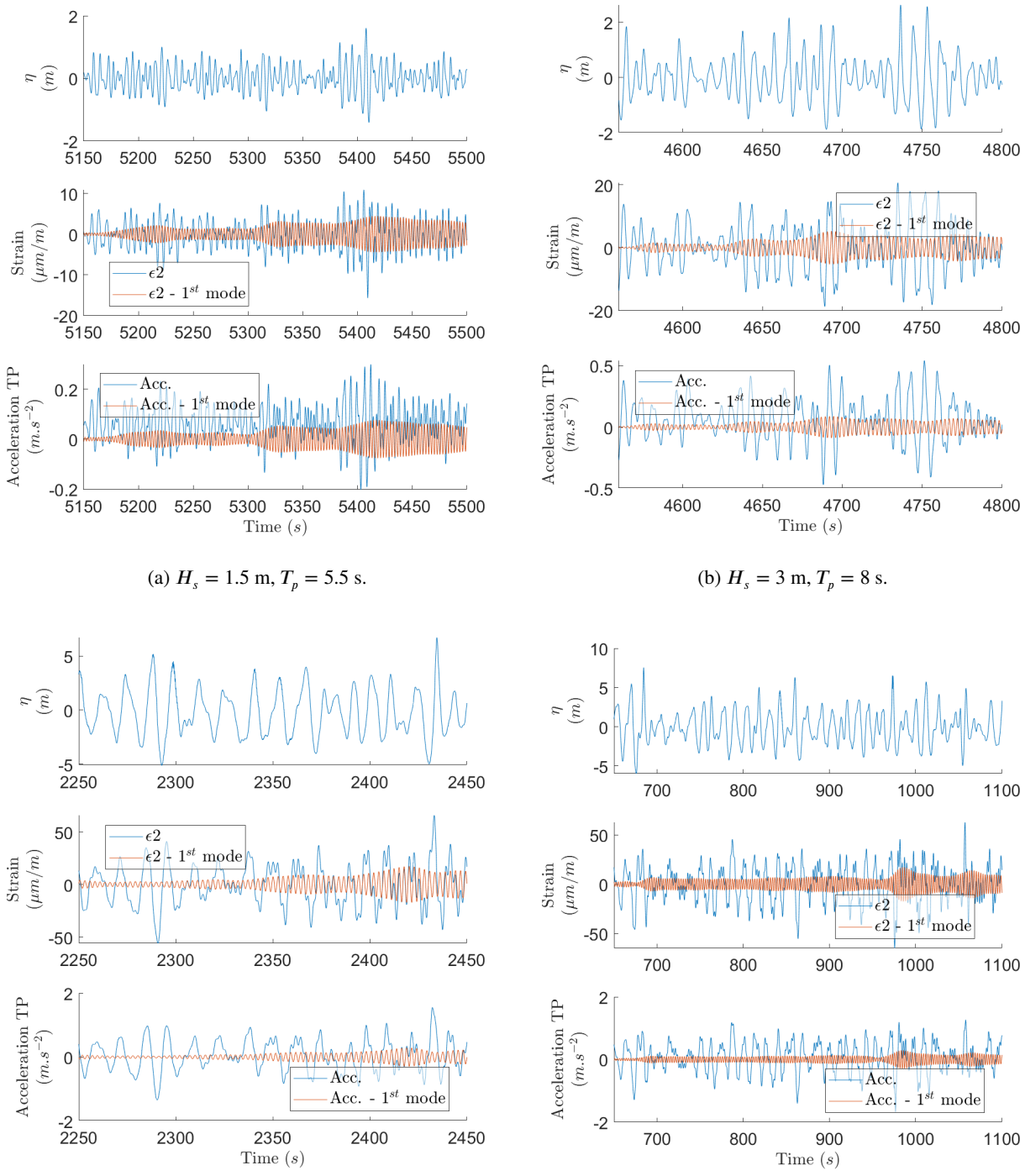

(a) H_s = 1.5 m, T_p = 5.5 s.

(b) H_s = 3 m, T_p = 8 s.

(c) H_s = 10.9 m, T_p = 13.8 s.

(d) H_s = 10.9 m, T_p = 13.8 s.

Figure 16: Resonance detection in several sea-states. In each case, the figures display the free surface elevation, the measured strain in $\epsilon 2$ (total, and band-pass filtered around the bending mode frequency) and the acceleration at the TP above the platform top.

ably due to second-order hydrodynamic loads, in the range of sum-frequency forces. The amplitude of the strain measured on the model may not be relevant when up-scaled, but this study proves that substantial resonant response can be excited with nonlinear hydrodynamic forces.

In stronger sea-states, and particularly in the 50-year return period conditions, ringing and springing responses were also observed, with significant amplitude. The vibrations are here probably induced by high-order hydrodynamic loads. This emphasizes that fatigue loading and damage should be

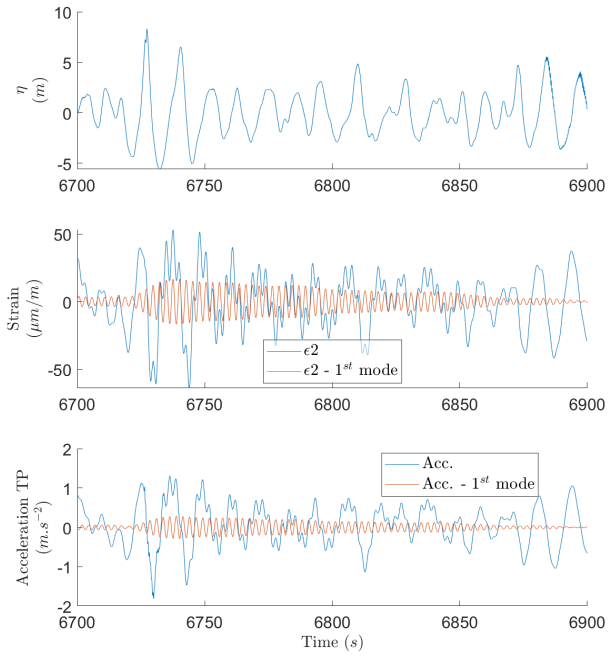

Figure 17: Ringing event after a wave impact in the sea-state 8 ($H_s = 10.9$ m, $T_p = 13.8$ s).

investigated including strongly nonlinear hydrodynamic effects. The conditions in the selected site (Gulf of Maine) can be described as medium intensity [9]. A future study should try to consider a more energetic site. Eventually, including aero-elastic effects (using SIL approaches, for instance) and their interaction with the hydro-elastic response should also be considered.

The collected data is also relevant for validation purposes, particularly for nonlinear hydrodynamic simulation tools dedicated to floating wind turbine and the structural response of their platform.

5. Acknowledgements

This work was carried out within the framework of the WEAMEC, West Atlantic Marine Energy Community, and with funding from the Pays de la Loire Region and Europe (European Regional Development Fund).

The authors thank Christian Berhault for the interesting discussions.

References

[1] Arnal, V., 2020. Modélisation expérimentale d'une éolienne flottante par une approche "software-in-the-loop". Ph.D. thesis. Ecole Centrale de Nantes.

[2] Bachynski, E.E., Kristiansen, T., Thys, M., 2017. Experimental and numerical investigations of monopile ringing inirregular finite-depth water waves. Applied Ocean Research 68, 154–170. URL: https://www.sciencedirect.com/science/article/pii/S0141118716305284, doi:10.1016/j.apor.2017.08.011.

[3] Bachynski, E.E., Thys, M., Dadmarzi, F.H., 2020. Observations from hydrodynamic testing of a flexible, large-diameter monopile in irregular waves. Journal of Physics: Conference Series 1669, 012028. URL: https://iopscience.iop.org/article/10.1088/1742-6596/1669/1/012028/pdf, doi:10.1088/1742-6596/1669/1/012028.

[4] Bachynski, E.E., Thys, M., Delhaye, V., 2019. Dynamic response of a monopile wind turbine in waves: Experimental uncertainty analysis for validation of numerical tools. Applied Ocean Research 89, 96–114. URL: https://www.sciencedirect.com/science/article/pii/S014111871830542X, doi:10.1016/j.apor.2019.05.002.

[5] Bak, C., Zahle, F., Bitsche, R., Taeseong, K., Yde, A., Henriksen, L.C., Hansen, M.H., Blasques, J.P.A.A., Gaunaa, M., Natajaran, A., 2013. The dtu 10-mw reference wind turbine.

[6] Borg, M., Bredmose, H., Hansen, A.M., 2017. Elastic deformations of floaters for offshore wind turbines dynamic modelling and sectional load calculations, in: Proceedings of the ASME 2017 36th International Conference on Ocean, Offshore and Arctic Engineering, OMAE2017, June 25-30, 2017, Trondheim, Norway, p. V010T09A044. doi:10.1115/OMAE2017-61446.

[7] Bouscasse, B., Merrien, A., Horel, B., De Hauteclocque, G., 2021. Experimental analysis of wave-induced vertical bending moment in steep regular waves. Journal of Fluids and Structures [submitted] .

[8] Faltinsen, O.M., Newman, J.N., Vinje, T., 1995. Nonlinear wave loads on a slender vertical cylinder. Journal of Fluid Mechanics 289, 179–198. URL: https://www.cambridge.org/core/journals/journal-of-fluid-mechanics/article/nonlinear-wave-loads-on-a-slender-vertical-cylinder/E11DCE48EF4B765A95C0C9296BDE00FC, doi:10.1017/S0022112095001297.

[9] Gomez, P., Sanchez, G., Llana, A., Gonzales, G., 2015. Deliverable 1.1. Oceanographic and meteorological conditions for the design. Technical Report. LIFES50+. URL: http://lifes50plus.eu/wp-content/uploads/2015/12/GA_640741_LIFES50-_D1.1.pdf.

[10] Goupee, A.J., Koo, B.J., Kimball, R.W., Lambrakos, K.F., Dagher, H.J., 2014. Experimental comparison of three floating wind turbine concepts. Journal of Offshore Mechanics and Arctic Engineering 136. URL: https://asmedigitalcollection.asme.org/offshoremechanics/article/136/2/020906/375202?casa_token=pYYzIjC2Y34AAAAA:KeQ4tz4V5v-i8SbWOjzJa4nB42dx8broJGVcNMQaTxuw1wXh9by0TP2B18EEAf200RT1y7Rj, doi:10.1115/1.4025804.

[11] Guignier, L., Courbois, A., Mariani, R., Choisnet, T., 2016. Multibody modelling of floating offshore wind turbine foundation for global loads analysis, in: Proceedings of the 26th International Ocean and Polar Engineering Conference, Rhodes, Greece, June 26-July 1.

[12] Gurley, K.R., Kareem, A., 1998. Simulation of ringing in offshore systems under viscous loads. Journal of Engineering Mechanics 124, 582–586. doi:10.1061/(ASCE)0733-9399(1998)124:5(582).

[13] Hegseth, J.M., Bachynski, E.E., 2019. A semi-analytical frequency domain model for efficient design evaluation of spar floating wind turbines. Marine Structures 64, 186–210. URL: https://www.sciencedirect.com/science/article/pii/S0951833918303149, doi:10.1016/j.marstruc.2018.10.015.

[14] Horel, B., Bouscasse, B., Merrien, A., Hauteclocque, G., 2019. Experimental assessment of vertical shear force and bending moment in severe sea conditions, in: of Mechanical Engineers, A.S. (Ed.), International Conference on Offshore Mechanics and Arctic Engineering, p. V003T02A031.

[15] Hsu, C.G., 2019. Substructure models for dynamic analysis of floating wind turbines and the effect of hull flexibility. Master's thesis. Delft University of Technology (TU Delft), Norwegian University of Science and Technology (NTNU). URL: http://resolver.tudelft.nl/uuid:5b3e0987-5ddb-4741-8442-791f8c04a297.

[16] ITTC, 2011. Global loads seakeeping procedure. 7.5-02-07-02.6.

[17] Jonkman, J., Musial, W., 2010. Offshore Code Comparison Collaboration (OC3) for IEA Task 23 Offshore Wind Technology and Deployment (No. NREL/TP-5000-48191). Technical Report.

[18] Jonkman, J.M., Matha, D., 2011. Dynamics of offshore floating wind turbines - analysis of three concepts. Wind Energy 14, 557–569. URL: https://onlinelibrary.wiley.com/doi/full/10.1002/we.

442, doi:10.1002/we.442.

[19] Kristiansen, T., Faltinsen, O.M., 2017. Higher harmonic wave loads on a vertical cylinder in finite water depth. Journal of Fluid Mechanics 833, 773–805. URL: https://www.cambridge.org/core/journals/journal-of-fluid-mechanics/article/higher-harmonic-wave-loads-on-a-vertical-cylinder-in-finite-water-depth/D7A563005EF0F28B7F55FAC708C6BB20, doi:10.1017/jfm.2017.702.

[20] Le Méhauté, B., 1976. An introduction to hydrodynamics and water waves. Springer Science and Business Media.

[21] Leroy, V., Bachynski-Polić, E.E., Babarit, A., Ferrant, P., Gilloteaux, J.C., 2021. A weak-scatterer potential flow theory-based model for the hydroelastic analysis of offshore wind turbine substructures. Ocean Engineering 238, 109702. doi:10.1016/j.oceaneng.2021.109702.

[22] Luan, C., Gao, Z., Moan, T., 2017. Development and verification of a time-domain approach for determining forces and moments in structural components of floaters with an application to floating wind turbines. Marine Structures 51, 87–109. doi:10.1016/j.marstruc.2016.10.002.

[23] Luan, C., Gao, Z., Moan, T., 2018. Comparative analysis of numerically simulated and experimentally measured motions and sectional forces and moments in a floating wind turbine hull structure subjected to combined wind and wave loads. Engineering Structures 177, 210–233. doi:10.1016/j.engstruct.2018.08.021.

[24] Malenica, Š., Molin, B., 1995. Third-harmonic wave diffraction by a vertical cylinder. Journal of Fluid Mechanics 302, 203–229. URL: https://www.cambridge.org/core/journals/journal-of-fluid-mechanics/article/thirdharmonic-wave-diffraction-by-a-vertical-cylinder/24FE56BF04F0BF348D7DE996869BC00D, doi:10.1017/S0022112095004071.

[25] Rienecker, M.M., Fenton, J.D., 1981. A fourier approximation method for steady water waves. Journal of Fluid Mechanics 104, 119–137. URL: https://www.cambridge.org/core/journals/journal-of-fluid-mechanics/article/fourier-approximation-method-for-steady-water-waves/E9F676C61D4D793AF4090254CA02E565, doi:10.1017/S0022112081002851.

[26] Robertson, A., Jonkman, J., Vorpahl, F., Popko, W., Qvist, J., Frøyd, L., Chen, X., Azcona, J., Uzunoglu, E., Guedes Soares, C., Luan, C., Yutong, H., Pengcheng, F., Yde, A., Larsen, T., Nichols, J., Buils, R., Lei, L., Anders Nygard, T., Manolas, D., Heege, A., Ringdalen Vatne, S., Ormberg, H., Duarte, T., Godreau, C., Fabricius Hansen, H., Wedel Nielsen, A., Riber, H., C., L.C., Abele, R., Beyer, F., Yamaguchi, A., K., J.J., Shin, H., Shi, W., Park, H., Alves, M., Guérinel, M., 2014. Offshore code comparison collaboration continuation within IEA wind task 30: Phase II results regarding a floating semisubmersible wind system (No. NREL/CP-5000-61154). Technical Report.

[27] Robertson, A.N., Wendt, F., Jonkman, J.M., Popko, W., Dagher, H., Gueydon, S., Qvist, J., Vittori, F., Azcona, J., Uzunoglu, E., Soares, C.G., Harries, R., Yde, A., Galinos, C., Hermans, K., de Vaal, J.B., Bozonnet, P., Bouy, L., Bayati, I., Bergua, R., Galvan, J., Mendikoa, I., Sanchez, C.B., Shin, H., Oh, S., Molins, C., Debruyne, Y., 2017. OC5 project phase II: Validation of global loads of the DeepCwind floating semisubmersible wind turbine. Energy Procedia 137, 38–57. URL: https://www.sciencedirect.com/science/article/pii/S1876610217352931, doi:10.1016/j.egypro.2017.10.333.

[28] Scolan, Y.M., Le Boulluec, M., Chen, X.B., Deleuil, G., Ferrant, P., Malenica, Š., Molin, B., 1997. Some results from numerical and experimental investigations on the high frequency responses of offshore structure, in: BOSS, pp. 127–142. URL: https://www.osti.gov/etdeweb/biblio/634770.

[29] Skaare, B., Nielsen, F.G., Hanson, T.D., Yttervik, R., Havmøller, O., Rekdal, A., 2014. Analysis of measurements and simulations from the hywind demo floating wind turbine. Wind Energy 18, 1105–1122. doi:10.1002/we.1750.

[30] Silva de Souza, C.E., Bachynski, E.E., 2018. Effects of hull flexibility on the structural dynamics of a tlp floating wind turbine, in: ASME 2018 37th International Conference on Ocean, Offshore and Arctic Engineering. American Society of Mechanical Engineers Digital Collection. URL: https://asmedigitalcollection.asme.org/OMAE/proceedings-abstract/OMAE2018/51319/V010T09A071/278206, doi:10.1115/OMAE2018-77310.

[31] Suja-Thauvin, L., Bachynski, E.E., Pierella, F., Borg, M., Krokstad, J.R., Bredmose, H., 2020. Critical assessment of hydrodynamic load models for a monopile structure in finite water depth. Marine Structures 72, 102743. URL: https://www.sciencedirect.com/science/article/pii/S095183392030037X?via%3Dihub, doi:10.1016/j.marstruc.2020.102743.

[32] Suzuki, H., Xiong, J., Do Carmo, L.H.S., Vieira, D.P., De Mello, P.C., Malta, E.B., Simos, A.N., Hirabayashi, S., Gonçalves, R.T., 2019. Elastic response of a light-weight floating support structure of fowt with guywire supported tower. Journal of Marine Science and Technology 24, 1015–1028. doi:10.1007/s00773-018-0614-7.

[33] Tomasicchio, G.R., Avossa, A.M., Riefolo, L., Ricciardelli, F., Musci, E., D'Alessandro, F., Vicinanza, D., 2017. Dynamic modelling of a spar buoy wind turbine, in: Proceedings of the ASME 2017 36th International Conference on Ocean, Offshore and Arctic Engineering, OMAE2017, June 25-30, 2017, Trondheim, Norway, p. V010T09A083. doi:10.1115/OMAE2017-62246.

[34] Wen, B., Li, Z., Jiang, Z., Peng, Z., Dong, X., Tian, X., 2020. Experimental study on the tower loading characteristics of a floating wind turbine based on wave basin model tests. Journal of Wind Engineering and Industrial Aerodynamics 207, 104390. doi:10.1016/j.jweia.2020.104390.

[35] Xu, K., Shao, Y., Gao, Z., Moan, T., 2019a. A study on fully nonlinear wave load effects on floating wind turbine. Journal of Fluids and Structures 88, 216–240. doi:10.1016/j.jfluidstructs.2019.05.008.

[36] Xu, K., Zhang, M., Shao, Y., Gao, Z., Moan, T., 2019b. Effect of wave nonlinearity on fatigue damage and extreme responses of a semi-submersible floating wind turbine. Applied Ocean Research 91, 101879. doi:10.1016/j.apor.2019.101879.